Lithiated carbon fibres for structural batteries characterised with Auger electron spectroscopy

(article starts on next page)

Full Length Article

Lithiated carbon fibres for structural batteries characterised with Auger electron spectroscopy

Marcus Johansen [*], Johanna Xu , Pui Lam Tam , Leif E. Asp , Fang Liu

Department of Industrial and Materials Science, Chalmers University of Technology, 412 96 Gothenburg, Sweden

ABSTRACT

Structural batteries are multifunctional devices that store energy and carry mechanical load, simultaneously. The pivotal constituent is the carbon fibre, which acts as not only structural reinforcement, but also as electrode by reversibly hosting Li ions. Still, little is known about how Li and carbon fibres interact. Here we map Li inserted in polyacrylonitrile based carbon fibres with Auger electron spectroscopy (AES). We show that with slow charge/discharge rates, Li distributes uniformly in the transverse and longitudinal direction of the fibre, and when fully discharged, all Li is virtually expelled. With fast rates, Li tends to be trapped in the core of the fibre. In some fibres, Li plating is found between the solid electrolyte interphase (SEI) and fibre surface. Our findings can guide AES analysis on other carbonaceous electrode materials for Li-ion batteries and be used to improve the performance of structural batteries.

1. Introduction

The electrification of transportation calls for lightweight and compact energy storage. A promising solution is to decrease the number of components by using multifunctional devices such as the structural battery, where the energy storage capabilities of traditional lithium-ion batteries are integrated into the structural components of carbon fibre reinforced composites [1–8]. In the structural battery, the carbon fibres, besides being the mechanical load carrier, simultaneously functions as negative electrodes by reversibly hosting lithium (Li) ions in their microstructure. Consequently, demands on electrochemical performance are imposed upon carbon fibres, which so-far have only been designed for structural purpose. To guide the development of carbon fibres tailored for multifunctional applications, it is evident that the fundamental knowledge of the interaction between Li and carbon fibres is required.

The microstructure of a carbon fibre is heterogenous, consisting of disordered domains and ordered domains of nano-sized crystallites. In the crystallites, graphene layers are stacked on top of each other in a turbostratic manner [9,10]. Li can either be inserted in the disordered domains or intercalated between the graphene layers in the crystallites [11]. In regards to electrochemical capacity of carbon fibres, previous research finds it advantageous to have microstructures with smaller crystallites, higher degree of disorder [11], and larger amount of

pyridinic and pyrrolic nitrogen heteroatoms [12]. During lithiation, due to insertion of Li, the fibre expands significantly in the transverse direction and moderately in the longitudinal direction. At the same time, the transverse elastic modulus increases, whereas the longitudinal elastic modulus decreases. During delithiation the fibre essentially reverts to its initial state [13]. The techniques – X-ray diffractometry (XRD), nuclear magnetic resonance (NMR) [14], Raman spectroscopy and synchrotron hard X-ray photoelectron spectroscopy (HAXPES) – that have been used up until now to study multifunctional carbon fibres, generate global information, which is often based on *multiple* fibres.

To understand how Li atoms are distributed within *individual* fibres with a diameter of ~5 μm, the lateral spatial resolution of the analysis technique needs to be in the sub-micrometre range. Techniques with sufficiently high spatial resolution that previously have been used to analyse lithium-containing materials are electron energy loss spectroscopy (EELS) coupled to transmission electron microscopy (TEM) [15,16], atom probe tomography (APT) [17–20], secondary ion mass spectroscopy (SIMS) [21,22], energy-dispersive X-ray spectroscopy (EDS) coupled to scanning electron microscopy (SEM) [23,24], and Auger electron spectroscopy (AES) [25–30]. Among them, AES is a technique that is well suited to analyse Li in a carbon fibre for the following reasons: its detection sensitivity to Li is high, since the signal yield of Auger electrons increases with decreasing atomic number [31]; the analysis is none-destructive; with ion sputtering, it can provide

---

composition depth profiles; sample preparation is relatively easy; the allowed sample size is large (in the cm range); the ultimate spatial resolution is high, ~10 nm; and it can distinguish between different species of Li [27,32].

In this paper, we utilise AES to analyse Li in polyacrylonitrile (PAN)-based carbon fibres, T800, with different states of lithiation and different charge rates. We compare with X-ray photoelectron spectroscopy (XPS) results. The interpretation of the Li-related fine structures in AES spectra can be applied in other carbonaceous battery materials. The results provide a holistic view of Li configuration and distribution in (de) lithiated carbon fibres. The insights gained will pave the way for the design of carbon fibres for multifunctional purposes.

2. Method

2.1. Material

PAN-based T800 carbon fibre tows spread to unidirectional ultra-thin tapes with a linear weight of 0.52 g/m (TeXtreme®, T800SC-12k-50C) were supplied by Oxeon AB. The as-received carbon fibres were attached with conductive silver paint to a copper current collector. Electrochemical half cells with lithium metal as counter electrode were manufactured with a pouch cell configuration. The pouch cell bags were laminated constructions of PET/Al/PE from Skultuna Flexible with layer thicknesses of 12 μm, 9 μm, and 75 μm, respectively. The separator was glass microfiber filter (Whatman GF/A, 260 μm thick). The electrolyte consisted of 1.0 M $LiPF_6$, ethylene carbonate (EC), and diethyl carbonate (DEC). Cell assembly was performed in dry argon atmosphere in a glove box (<1 ppm H_2O, <1 ppm O_2). Hereafter called uncycled carbon fibres were soaked in the electrolyte and assembled into a pouch cell for a duration of 90 h, corresponding to the time of five charge/discharge cycles.

Charge/discharge cycling was performed with a Neware CT-4008-5V10mA-164 battery cycler. Five cycles were conducted in the potential window between 1.5 V and 0.01 V versus Li/Li$^+$, with the former voltage considered to correspond to fully delithiated carbon fibres and the latter to fully lithiated ones. The galvanostatic cycles had a current corresponding to 0.1C based on the theoretic maximum capacity of graphite of 372 mAh/g, before the final discharge/charge current was set to correspond to 0.05C for slow charge rate and 0.2C rapid charge rate (Fig. S1). The cell potential corresponding to 50 % lithiation was determined after two cycles and set to 0.3 V.

Disassembly of the cells was conducted inside the glove box. The fibre tow was dried overnight in the inert atmosphere of the glove box. Then the tow was adhered to the sample holder of AES with a copper tape, which also created the conduction path to prevent charging issues in the AES. The tow was cut with a clean scissor. The fibres were transferred to the spectrometers in a transfer vessel without exposure to ambient air. SEM micrographs (Fig. S2) show extensive formation of oxides on a lithiated carbon fibre after unprotected transfer through ambient air from the glove box to the microscope, underscoring the importance of the transfer vessel to protect the sensitive lithiated carbon fibres.

2.2. Spectroscopy

AES analyses were performed in a PHI 700 Scanning Auger Nanoprobe, with a Schottky field emission electron source, and a cylindrical mirror analyser with energy resolution <0.6 %. For both secondary electron imaging and Auger spectrometric measurements, the accelerating voltage was set to 3 kV and the beam current to 1 nA, for which no beam damage was observed. For each cycle state, ten fibres were analysed. Spectra were collected between 10 and 700 eV with a step size of 1.0 eV. Layer-by-layer depth profiling was conducted with an argon (Ar) ion gun with 1 min sputtering at each interval for a total time of 120 min. The sputter rate was around 145 Å/min, with reference to the tantalum

oxide (Ta_2O_5) etch rate calibration. The concentration profiles in the transverse direction of carbon fibres were obtained with AES in two approaches: positioning the fibre with its lateral surface facing the incident electron beam, and alternate between analysis and ion sputtering; or positioning the fibres with their transverse cross-sections facing the incident electron beam, and then analysing across the cross-section (Fig. 1). The advantage with the former approach is that the depth resolution is high. The advantage of the latter is that the entire diameter can be scanned in a short time. The spatial resolution of the scan profile is limited by the size of the electron beam ~10 nm. However, to increase the yield of Auger electrons the analysis area was enlarged to ~350 nm, so that the 5 μm fibre cross-section was covered by 13 analysis points (six points to either side of a centre point). MultiPak software (Version 9.7.0.1) was used to differentiate AES data and smooth the data with Savitzky-Golay filter. XPS measurements were performed in a PHI 5000 VersaProbe III Scanning X-ray Microprobe with a monochromatic AlKα ($\hbar\nu$ = 1486.6 eV) source with a beam size ~100 μm. During narrow scan for selected elements of interest, pass energy was set to 26.0 eV and the step size to 0.10 eV. MultiPak was also used to conduct peak deconvolution of XPS data.

3. Results and discussion

AES spectra were acquired from the lateral surface of lithiated carbon fibres. The AES Li$_{KLL}$ signal consists of three distinct peaks at 35 eV, 45 eV, and 55 eV (Fig. 2a). In contrast, the Li1s signal from XPS only consists of one single peak (Fig. S3), where deconvolution is required to identify the chemical states. It is evident that in case of analysing (de) lithiated carbonaceous materials, AES offers richer and more easily interpretable information of chemical configuration on Li than XPS. We show below how we assign the Li$_{KLL}$ peaks to their corresponding chemical configurations. The chemical state information available in AES spectra from lithium containing carbon materials can readily be used in carbon anode research.

By comparing the evolution of the Li$_{KLL}$ peaks with other detected elements during depth profiling, it was found that the 35 eV peak follows the same trend as the O$_{KLL}$ signal at 510 eV (Fig. 2b). Further connection between Li$_{KLL}$ at 35 eV and O is found when comparing AES spectra from a sputtered and an intact cross-sectional surface of a lithiated fibre. Without sputtering, Li, C, and O are detected and the 35 eV peak is present, but after sputtering, both O and the 35 eV peak disappear (Fig. S4). Sputtering removes the small amount of oxide on the surface of the lithiated fibres. This link between the low energy peak of Li$_{KLL}$ and the O$_{KLL}$ signal was used by Clausing and Easton to identify lithium oxide [33]. Evidently, 35 eV is associated with lithium bonded to oxygen (Li-O).

The 55 eV peak, however, does not follow any trend of other elements in the depth profile, which indicates that it is independent and thus presumably represents elemental lithium (Li^0). Indeed, this is confirmed by using high electron beam currents (10 nA) to severely bombard a lithiated carbon fibre. The overwhelming supply of electrons on the surface of the sample leads to local excess electrons. Immediate SEM monitoring shows a gradual formation of a precipitate on the fibre surface. Coinciding with the appearance of this precipitate, the shape of the Li$_{KLL}$ signal changes to be dominated by the 55 eV peak (Fig. 2c). The excess electrons lead to accumulation of lithium previously inserted into the fibre to form a precipitate of Li^0. Zhang *et al.* also showed how the electron bombardment can create precipitates of Li^0 [33,34]. Thus, the peak at 55 eV corresponds to Li^0.

The 45 eV peak follows the trend of the 260 eV peak of the C$_{KLL}$ signal (Fig. 2d). The C$_{KLL}$ signal consists of two peaks: the main peak at 275 eV is associated with carbon bonded to carbon, whereas the low energy peak at 260 eV is associated with carbon bonded to metal, in this case lithium (C-Li). Craig *et al.* demonstrated how additional low energy peaks from the C$_{KLL}$ signal appeared when carbon bonded to metals [35]. Thus, the 45 eV peak represents lithium bonded to carbon (Li-C).
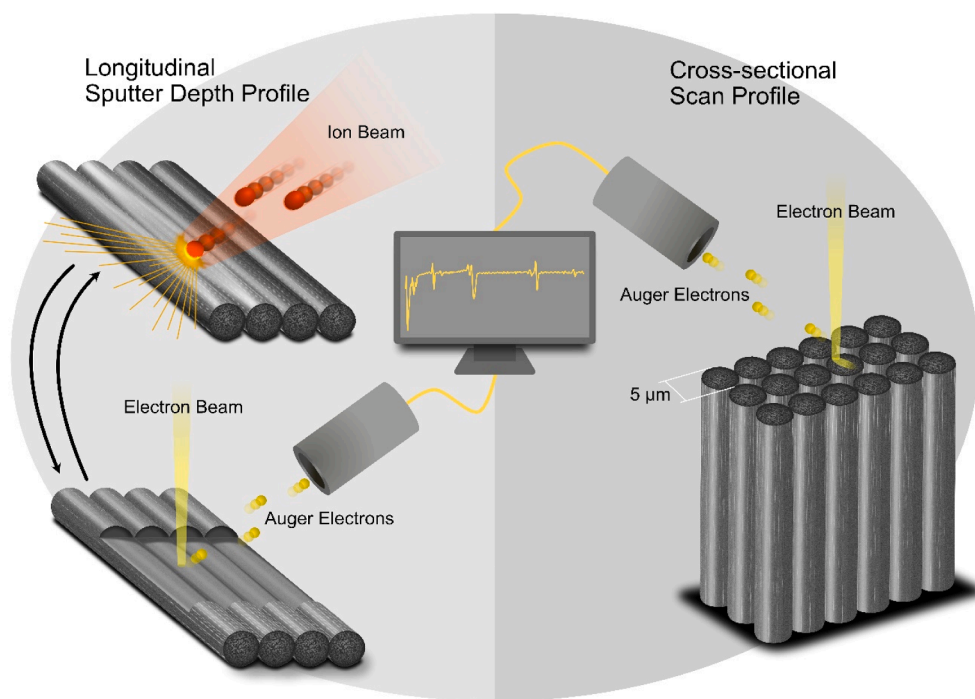
Fig. 1. Schematic of the two approaches to obtain concentration profiles along the transverse direction of carbon fibres. To the left, sputter depth profiling, where ion sputter and spectroscopic measurements alternate to generate a profile. To the right, cross-sectional scan profiling, where the electron beam scans across the fibre end and spectra are collected.

Furthermore, the C_{KLL} signal of lithiated carbon fibres also exhibit a fine feature at 280 eV. The C_{KLL} signal can be viewed as a convolution of σ and π bonds in the graphite lattice, as proposed by Murday *et al.* When Li intercalates in between two graphene layers [36], a Li atom located above a graphene ring donates an electron that occupies the antibonding π* band and give rise to the feature at the higher energy of 280 eV [37]. Since intercalation only takes place in ordered domains [11], the 280 eV feature can represent Li intercalated into the ordered domains of the carbon fibre. Interestingly, when the C_{KLL} signal of a fully lithiated carbon fibre and a fibre lithiated to 50 % of the electrochemical potential are compared (Fig. 3), it is found that the fully lithiated fibre shows the π* feature, whereas the 50 % lithiated fibre does not. This indicates that at increased charge states Li is located in both ordered and disordered domains, while at lower charge states, Li is mainly located in disordered domains. Similar conclusion was drawn by Fang *et al.* using X-ray diffractometry and nuclear magnetic resonance on lithiated carbon fibres [14]. It is important to note that the ordered domains in a carbon fibre have a turbostratic structure instead of a graphitic structure (hexagonal close packed). In turbostratic carbon, the graphene layers do not align above each other in an ordered way, and some atoms have sp^3 hybridization. Thus, Li intercalation between the layers is much disturbed. Endo et al. demonstrated that the intermediate level of order (between graphite and amorphous carbon) leads to a minimum in energy capacity compared to either more ordered or more disordered carbon. As the level of disorder grows, the intercalation process is replaced by a Li insertion process into the smaller and randomly located graphene layers [11,38]. This explains the preference of Li to first be inserted into the disordered domains of the carbon fibre.

Now, with a good understanding of the AES spectra, we can analyse the chemical composition of the cross-sectional and lateral surfaces of carbon fibres subjected to different electrochemical cycling conditions and compare the results with those of XPS (Fig. 4).

AES analysis across the cross-section of fully lithiated carbon fibres reveals that the Li/C intensity ratio is rather uniform across the transverse direction of the fibre (Fig. 4a). With 13 adjacent analysis regions on the ~5 μm wide cross-section, no preferential Li enriched region is

observed. Thus, the inserted Li at a charge rate of 0.05C is distributed evenly throughout the whole carbon fibre in the transverse direction. Furthermore, a fibre, which has been charged to 50 % of the electrochemical potential, also shows a uniform Li distribution, albeit with a lower Li/C ratio. When fully discharged down to 0 % of the electrochemical potential at a low discharge rate of 0.05C, the Li signal drops below the detection limit for AES, indicating that the delithiation process seemingly manages to expel all Li out of the carbon fibre. However, for the fully discharged fibres that are instead subjected to a more rapid discharge rate of 0.2C, still detectable quantities of Li remain in the fibres. Therefore, the concentration of remaining Li in fully discharged carbon fibres depends on the discharge rate. Additionally, at increased discharge rates the remaining Li is preferentially located at the inner part of the fibre. The reason can be a combination of the longer distance required for diffusing from the inner part and the inherent skin-core microstructure in the carbon fibres [39–41]. With increased charge/discharge rate, the battery capacity is reduced [2] as a result of limited mass transport and charge transfer [42], which decreases the rate of Li insertion/de-insertion to/from the carbon fibre. Furthermore, these rate limiting processes may behave differently at different stages of lithiation, and one of the reasons is the electrical conductivity increases for graphitic materials with intercalated Li [43]. The insights in Li distribution in carbon fibres as a function of charge state and charge rate are valuable for the future research on structural batteries in general, and particularly for the design of multifunctional carbon fibres.

AES sputter depth profiling on the lateral surface shows that a lithiated carbon fibre is encrusted by a thin layer of solid electrolyte interphase (SEI), which is indicated by a highly fluctuated region in the beginning of the depth profile before the fibre is reached and the intensity of the signals stabilises (Fig. 4b). SEI forms on the surface of carbonaceous anode materials through side reactions with electrolyte solvent and salt during the operation of Li-ion batteries and is essential to the battery performance [44]. AES detects C, Li, O, F, and P in the SEI, which consists of the complex reaction products of the electrolyte ($LiPF_6$, $OC(OCH_3)_2$, and $(CH_2O)_2CO$). When the SEI has been sputtered away the O, F, and P signals fade away and C and Li become the only
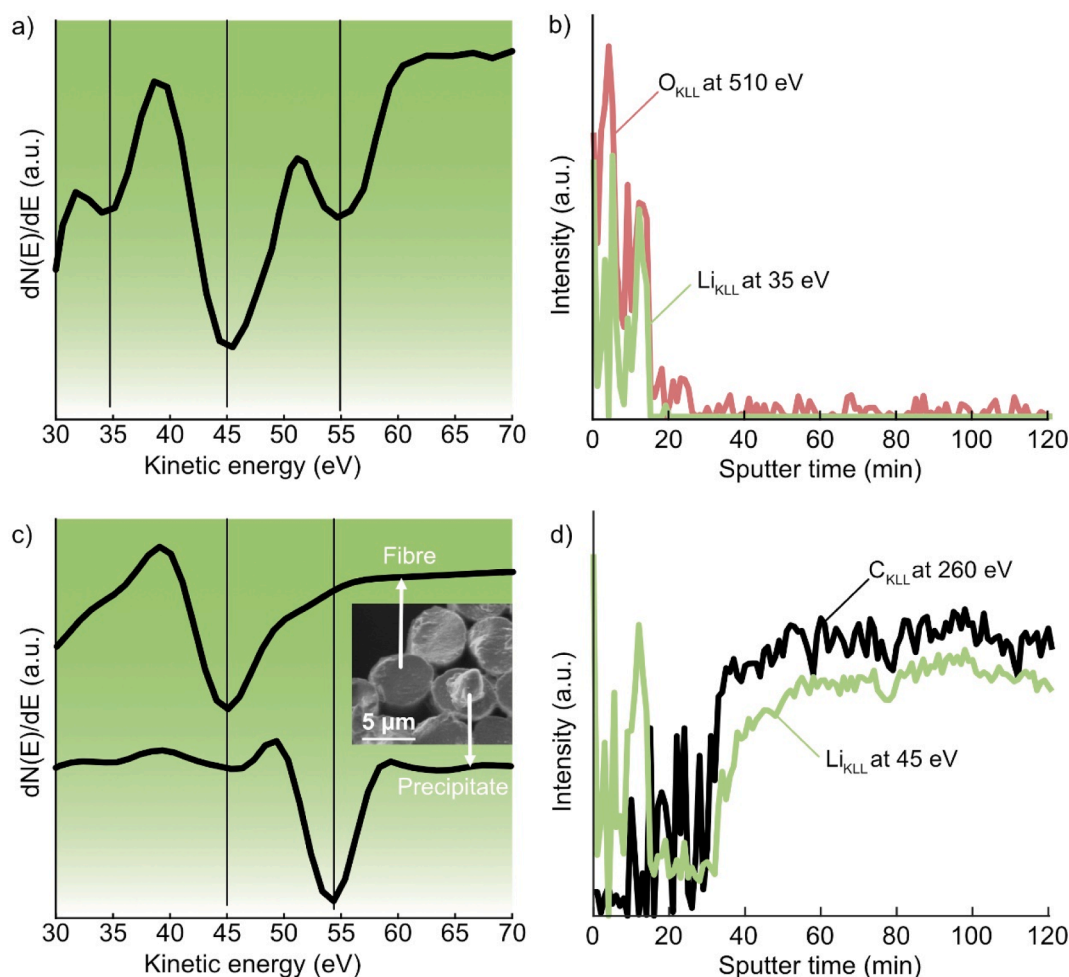
Fig. 2. Assignment of Li_{KLL} peaks. a) Differentiated Li_{KLL} signal with three peaks from the lateral surface of a lithiated carbon fibre. b) Depth profile of Li_{KLL} at 35 eV compared to O_{KLL} at 510 eV. They follow the same trend. c) Li_{KLL} signals at 45 eV from the interior of an intact fibre and at 55 eV from a precipitate formed under a high electron current. Inset, SEM micrograph showing the cross-section of lithiated carbon fibres, one of which was exposed to a high beam current (10 nA), which resulted in the formation of a precipitate on the surface. d) Depth profile of Li_{KLL} at 45 eV compared to C_{KLL} at 260 eV. Note that the intensity values in b) and d) are normalized individually.
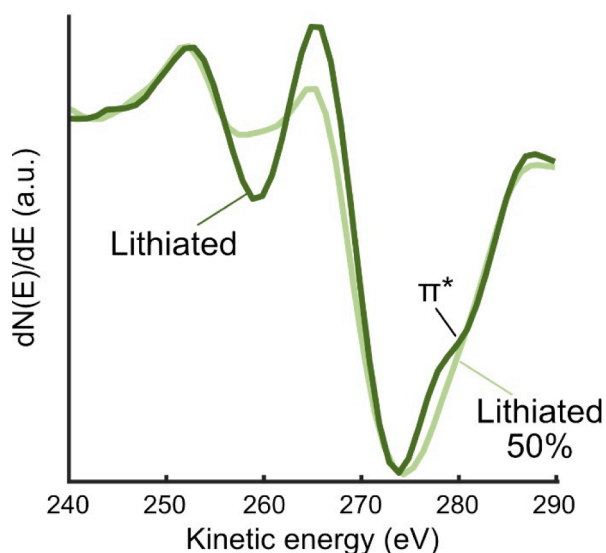
Fig. 3. C_{KLL} signal from a fully lithiated carbon fibre and a 50 % lithiated carbon fibre. The fully lithiated fibre has an additional fine feature at 280 eV representing the antibonding π* band.

elements present. Thus, it can be concluded that no co-insertion ozf O, P, and F along with Li is detected by AES. In the fibre region the relative intensities of C and Li stay constant, similarly as for the cross-section analysis in Fig. 4a, although the sputtering depth is only estimated to be ~1.5 μm.

Fig. 4c shows the AES survey spectra and Li_{KLL} and C_{KLL} signals of the surface SEI layer for lithiated, delithiated, and uncycled fibres. Uncycled fibres, even though they have been soaked in electrolyte for 90 h, yield only a main signal from C, and trace amounts of N. Both elements have been proved to belong to the carbon fibre [12]. After cycling, Li, P, O, and F are present, and N becomes undetectable by AES. The signals from the elements introduced after cycling are weaker in delithiated fibres than lithiated ones, especially the intensities of lithium bonded to carbon (45 eV and 260 eV), which indicates that the SEI changes during cycling [45]. Additionally, SEI thickness varies between lithiated and delithiated fibres, as shown by the depth profiles (Fig. S5).

Through deconvolution of C1s and O1s in XPS (Fig. 4d), it is found that the signals from Li_2CO_3 (C1s = 290 eV and O1s = 532.5 eV) in lithiated fibres are significantly stronger than in delithiated fibres. Li_2O (O1s = 529 eV) and (Li_2O_2 = 531.5 eV) are present for both types of lithiation state. On uncycled fibres, no Li_2O is detected, suggesting that the Li_2O found in lithiated and delithiated fibres is a product of the cycling.

Noteworthy is the discrepancy between AES and XPS spectrum of the
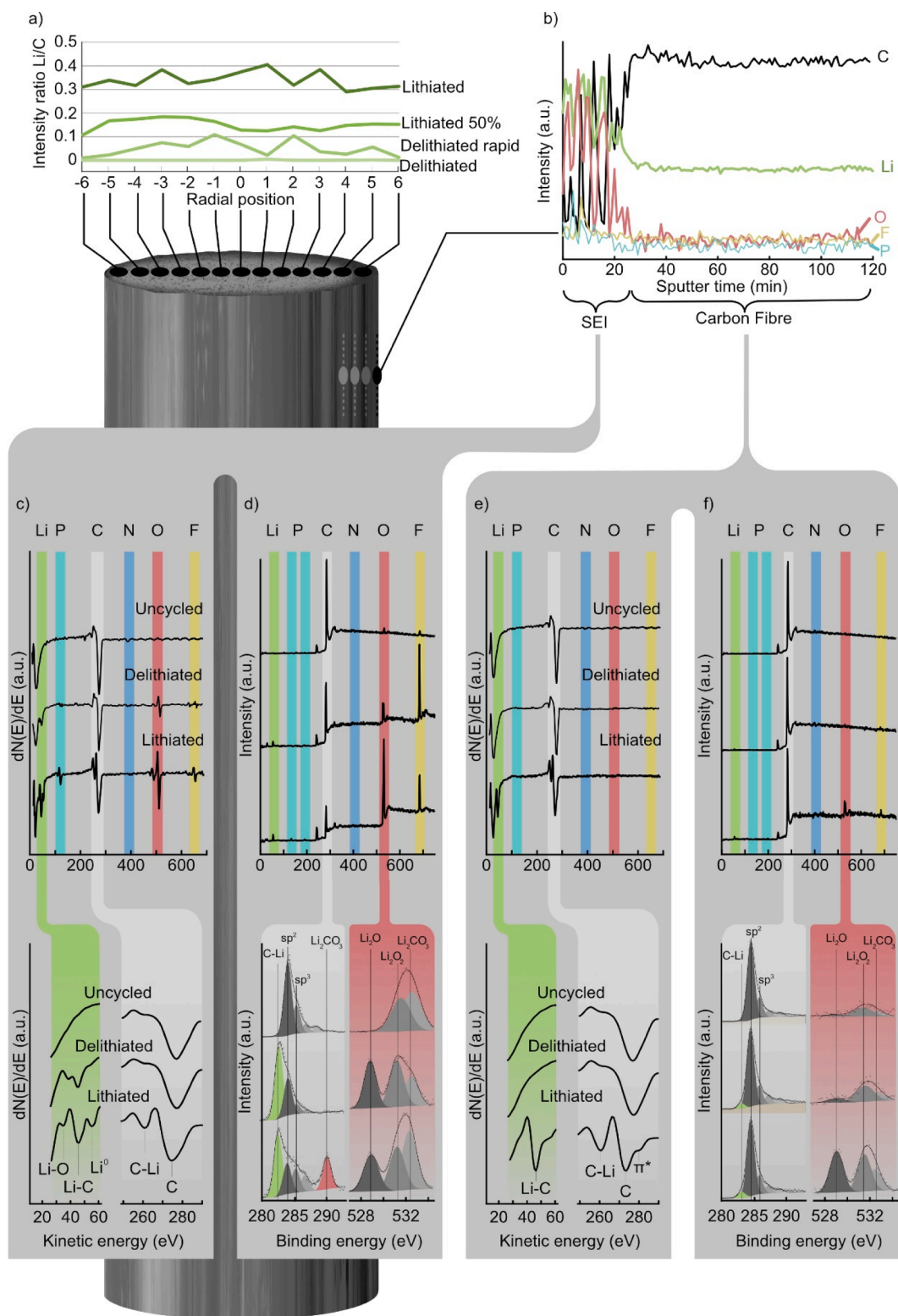
Fig. 4. Overview of AES and XPS results. a) Li/C intensity ratio measured by AES as a function of radial position in fibres with different charge states. b) AES sputter depth profile of a lithiated fibre. AES and XPS spectra of survey and narrow scan of Li$_{KLL}$ and C$_{KLL}$ (AES) and C1s and O1s (XPS) from c-d) the SEI region and (e-f) the fibre region.

surface of uncycled fibres, where the former shows no signal other than C and N (Fig. 4c), while the latter shows small but clear signals from O and F (Fig. 4d). This can be explained by the high lateral resolution (~10 nm) of AES, which allows information to be obtained only from inside individual fibres, while the analysis area of the XPS (beam diameter of ~100 μm) covers multiple fibres as well as the boundaries between the fibres. There it is likely that electrolyte residues gather and then contributes to the XPS spectrum in a way it does not for AES. Still, there are also sources of uncertainty in the AES analysis. Firstly, for each cycling condition ten fibres were investigated. A larger sample size

would provide better statistics, however, the data retrieved is deemed representative. Further uncertainty may arise from the slightly uneven topography of the cross-section surfaces. Therefore, only the flattest cross-section surfaces were selected and investigated. additional transfer between instruments imposes unacceptable risks of contamination. Finally, the fibres were selected randomly within the fibre tow, which means that there is variation in the distance between the fibres and the lithium source. Nevertheless, the tow thickness is only ~25 μm and all fibres are in direct contact with the liquid electrolyte, which is assumed to negate any concentration gradients within the fibre tow. However, in a structural battery electrolyte (a hybrid polymer and liquid electrolyte system) with significantly lower ion conductivity, fibre position may have far-reaching effects.

After sputtering down to the fibre region of the lithiated fibres, only C and Li is present in the AES spectrum (Fig. 4e). The Li_{KLL} signal only exhibits the Li-C peak at 45 eV, indicating that Li is bonded to C. The C_{KLL} signal consists of peaks at 260 and 275 eV, as well as the fine feature at 280 eV. The delithiated and uncycled fibres are remarkably similar, showing no Li_{KLL} and only one carbon peak in C_{KLL}, which reaffirms that the delithiation process at low discharge rates expels most of the Li out of the carbon fibres, and any remaining level of Li is below the detection limit of AES. Based on studies with higher charge rates, it was previously assumed that capacity losses are associated with trapped Li in the carbon fibres [1]. However, at the low charge rate in this study, no significant amount of Li gets trapped inside the carbon fibres, while Li is still found retained on the surface of these fibres and in the SEI. Thus, multiple regions can trap Li and be responsible for capacity losses.

It has been showed that when the ratio of sp^2 and sp^3 carbon changes, the distance between the local minima and maxima of C_{KLL} also changes [46–48]. The similarity in the shape of C_{KLL} for delithiated and uncycled fibres (Fig. 4e) suggests that no permanent change in the carbonaceous structure has occurred during the cycling. Further evidence of this structural stability to cycling is seen in the deconvolution of C1s in the XPS spectra (Fig. 4f), where the sp^2/sp^3 ratio remains constant for all types of cycling conditions.

Discrepancies between AES and XPS is also found for the fibre region (Fig. 4e and 4f). AES reveals no O or F, whereas XPS does. Additionally, AES registers no Li in delithiated fibres, while XPS registers a lithium carbide signal at the low energy end of the C1s, at 282.5 eV. Once again, the reason is most probably the much larger analysing area in XPS. The Li, O and F detected by XPS likely comes from electrolyte residues in the crevices between the fibres that were not thoroughly sputtered away. XPS is useful to analyse the composition of the SEI on cycled carbon fibres as deconvolution of the O1s signal can yield much more chemical state information than the O_{KLL} signal from AES can, but for Li mapping in carbon fibres, the high lateral resolution (small analysis area) of AES is needed.

The possible variation in Li distribution along the same fibre and between different fibres was analysed using AES. Sputter depth profiles were compared at four positions along fully lithiated carbon fibres with interspacing of 2 μm between each position. It shows remarkably little variation longitudinally within the same fibre (Fig. S6). For each individual fibre the SEI thickness remains similar along the fibre. Likewise, in the fibre region the Li/C intensity ratio is at a similar level from position to position, implying a fully lithiated fibre has an even Li distribution along the fibre axis on the micrometre scale.

In Fig. 5, typical depth profiles of three adjacent fibres in the same tow are compared. For all three fibres, again the Li/C intensity ratios are at a similar level, meaning that the amount of Li stored by individual fibres is comparable. However, the SEI thickness varies. For two of the fibres on the side, the SEI thickness is thin (Fig. 5a and 5c), whereas for the one in the middle, the thickness is almost three times thicker (Fig. 5b). This much larger thickness in the fibre is accompanied by an additional intermediate region between the SEI and fibre, yielding a strong signal from Li^0. This indicates Li plating along the fibre, and it is found at all four measurement positions (Fig. S6). Li plating is a major cause for capacity decay in Li-ion batteries, as dead Li is accumulated on the anode surface and becomes inactive [49]. The reason why some fibres exhibit plating while others do not is unclear. However, it is evident that not all fibres behave the same. Therefore, even though, at the end of full charging, different fibres manage to hold the same amount of lithium, they may behave differently during cycling, since the SEI impacts the transport of Li-ions [44]. This heterogeneity between fibres has not been reported before. The finding gives a new potential design parameter for structural batteries.

4. Conclusion

The power of AES as an analysis tool for electrochemically (dis) charged carbon fibres was demonstrated. It allows both inter- and intra-fibre investigation due to the large sample size and high lateral and depth resolution. More importantly, it can distinguish the different chemical configurations of metallic lithium Li^0, Li-O and Li-C bond, and even the π* bonding, which implies the intercalation of Li into the ordered graphene layers. XPS is a useful complement, but the spatial resolution is too low relative the fibre diameter, and the acquired data tend to contain information from possible remained contaminations.

AES and XPS were utilised to reveal Li distribution and configuration in carbon fibres for structural batteries. Fully charged carbon fibres have a rather uniform spatial distribution of Li in the transverse and longitudinal direction of the fibre. Li is located in both ordered and disordered domains based on the fine structure of π* signal. Carbon fibres lithiated to 50 % still show uniform Li distribution, but Li is located foremost in disordered domains. In fibres discharged to 0 % at a slow discharge rate of 0.05C, the Li content is below the detectable level, whereas with a rapid discharge rate 0.2C, some Li is trapped mainly in
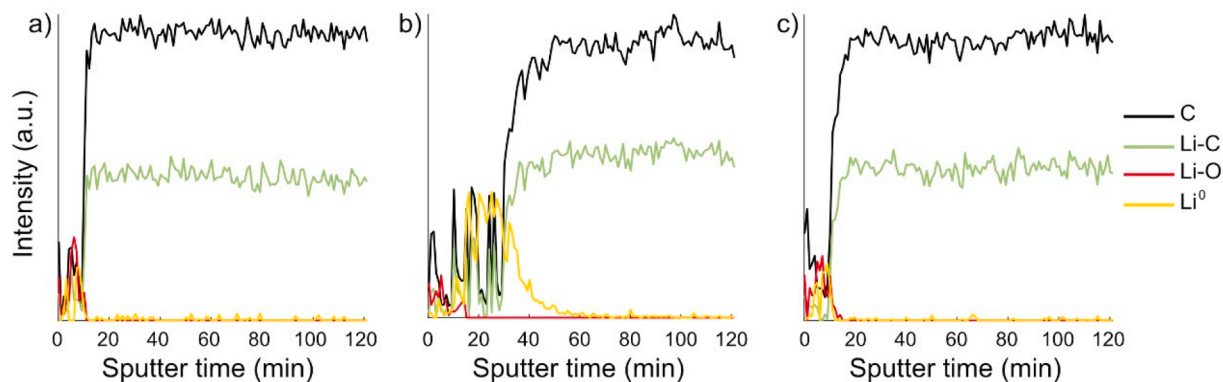

Fig. 5. AES depth profiles from three adjacent lithiated carbon fibres lying side by side. Fibres on the side a) and c) have a thin SEI layer. The fibre in the middle b) with a thick SEI layer and Li plating.

the core of the fibre. The cycled fibres are covered by a layer of SEI. The SEI thickness and composition vary from fibre to fibre in the same tow. Some fibres exhibit Li plating between the SEI layer and the fibre surface, while their adjacent fibres do not.

The detailed AES spectrum analysis presented here can be generalised to interpret other carbon-based anodes for Li-ion batteries to reveal the rich chemical information. Additionally, this study provides new insights into how Li is distributed in carbon fibres used in structural batteries. This knowledge can aid tailoring of future carbon fibre microstructures for multifunctional structural batteries.

CRediT authorship contribution statement

Marcus Johansen: Conceptualization, Methodology, Software, Validation, Formal analysis, Investigation, Writing – original draft, Visualization. **Johanna Xu:** Methodology, Investigation, Writing – review & editing. **Pui Lam Tam:** Investigation, Resources, Writing – review & editing. **Leif E. Asp:** Resources, Writing – review & editing, Funding acquisition. **Fang Liu:** Conceptualization, Methodology, Writing – original draft, Supervision, Project administration, Funding acquisition.

Declaration of Competing Interest

The authors declare that they have no known competing financial interests or personal relationships that could have appeared to influence the work reported in this paper.

Data availability

Data will be made available on request.

Acknowledgement

Appendix A. Supplementary data

Supplementary data to this article can be found online at https://doi.org/10.1016/j.apsusc.2023.157323.

References

[1] L.E. Asp, M. Johansson, G. Lindbergh, J. Xu, D. Zenkert, Structural battery composites: a review, Funct. Compos. Struct. 1 (2019), https://doi.org/10.1088/2631-6331/ab5571.

[2] L.E. Asp, K. Bouton, D. Carlstedt, S. Duan, R. Harnden, W. Johannisson, M. Johansen, M.K.G. Johansson, G. Lindbergh, F. Liu, K. Peuvot, L.M. Schneider, J. Xu, D. Zenkert, A Structural Battery and its Multifunctional Performance, Adv. Energy Sustain. Res. 2000093 (2021), https://doi.org/10.1002/aesr.202000093.

[3] J. Xu, Z. Geng, M. Johansen, D. Carlstedt, S. Duan, T. Thiringer, F. Liu, L.E. Asp, A multicell structural battery composite laminate, EcoMat. 4 (2022) 1–11, https://doi.org/10.1002/eom2.12180.

[4] L.E. Asp, E.S. Greenhalgh, Structural power composites, Compos. Sci. Technol. 101 (2014) 41–61, https://doi.org/10.1016/j.compscitech.2014.06.020.

[5] W. Johannisson, D. Zenkert, G. Lindbergh, Model of a structural battery and its potential for system level mass savings, Multifunct. Mater. 2 (2019), https://doi.org/10.1088/2399-7532/ab3bdd.

[6] C. Meng, N. Muralidharan, E. Teblum, K.E. Moyer, G.D. Nessim, C.L. Pint, Multifunctional Structural Ultrabattery Composite, Nano Lett. 18 (2018) 7761–7768, https://doi.org/10.1021/acs.nanolett.8b03510.

[7] K. Moyer, C. Meng, B. Marshall, O. Assal, J. Eaves, D. Perez, R. Karkkainen, L. Roberson, C.L. Pint, Carbon fiber reinforced structural lithium-ion battery composite: Multifunctional power integration for CubeSats, Energy Storage Mater. 24 (2020) 676–681, https://doi.org/10.1016/j.ensm.2019.08.003.

[8] T. Jin, G. Singer, K. Liang, Y. Yang, Structural batteries: Advances, challenges and perspectives, Mater. Today. (2022), https://doi.org/10.1016/j.mattod.2022.12.001.

[9] J.-B. Donnet, T.W. Wang, S. Rebouillat, J.C.M. Peng, Carbon fibres, third ed., Marcel Dekker Inc., 1998.

[10] S. Park, Carbon Fibers, second ed., Springer Nature, 2018.

[11] G. Fredi, S. Jeschke, A. Boulaoued, J. Wallenstein, M. Rashidi, F. Liu, R. Harnden, D. Zenkert, J. Hagberg, G. Lindbergh, P. Johansson, L. Stievano, L.E. Asp, Graphitic microstructure and performance of carbon fibre Li-ion structural battery electrodes, Multifunct. Mater. 1 (2018), 015003, https://doi.org/10.1088/2399-7532/aab707.

[12] M. Johansen, C. Schlueter, P.L. Tam, L.E. Asp, F. Liu, Mapping nitrogen heteroatoms in carbon fibres using atom probe tomography and photoelectron spectroscopy, Carbon N. Y. 179 (2021) 20–27, https://doi.org/10.1016/j.carbon.2021.03.061.

[13] S. Duan, A.H.S. Iyer, D. Carlstedt, F. Rittweger, A. Sharits, C. Maddox, K.R. Riemschneider, D. Mollenhauer, M. Colliander, F. Liu, L.E. Asp, Effect of lithiation on the elastic moduli of carbon fibres, Carbon N. Y. 185 (2021) 234–241, https://doi.org/10.1016/j.carbon.2021.09.037.

[14] Y. Fang, K. Peuvot, A. Gratrex, E.V. Morozov, J. Hagberg, G. Lindbergh, I. Furó, Lithium insertion in hard carbon as observed by 7Li NMR and XRD. The local and mesoscopic order and their relevance for lithium storage and diffusion, J. Mater. Chem. A (2022) 10069–10082, https://doi.org/10.1039/d2ta00078d.

[15] F. Wang, J. Graetz, M.S. Moreno, C. Ma, L. Wu, V. Volkov, Y. Zhu, Chemical distribution and bonding of lithium in intercalated graphite: Identification with optimized electron energy loss spectroscopy, ACS Nano 5 (2011) 1190–1197, https://doi.org/10.1021/nn1028168.

[16] Z.W. Yin, W. Zhao, J. Li, X.X. Peng, C. Lin, M. Zhang, Z. Zeng, H.G. Liao, H. Chen, H. Lin, F. Pan, Advanced Electron Energy Loss Spectroscopy for Battery Studies, Adv. Funct. Mater. 32 (2022), https://doi.org/10.1002/adfm.202107190.

[17] S.H. Kim, S. Antonov, X. Zhou, L.T. Stephenson, C. Jung, A.A. El-Zoka, D.K. Schreiber, M. Conroy, B. Gault, Atom probe analysis of electrode materials for Li-ion batteries: Challenges and ways forward, J. Mater. Chem. A 10 (2022) 4926–4935, https://doi.org/10.1039/d1ta10050e.

[18] G.H. Greiwe, Z. Balogh, G. Schmitz, Atom probe tomography of lithium-doped network glasses, Ultramicroscopy 141 (2014) 51–55, https://doi.org/10.1016/j.ultramic.2014.03.007.

[19] J. Maier, B. Pfeiffer, C.A. Volkert, C. Nowak, Three-Dimensional Microstructural Characterization of Lithium Manganese Oxide with Atom Probe Tomography, Energy Technol. 4 (2016) 1565–1574, https://doi.org/10.1002/ente.201600210.

[20] B. Pfeiffer, J. Maier, J. Arlt, C. Nowak, In Situ Atom Probe Deintercalation of Lithium-Manganese-Oxide, Microsc. Microanal. 23 (2017) 314–320, https://doi.org/10.1017/S1431927616012691.

[21] B. Rais, E.T. Ostrowski, A. Canton, C.H. Skinner, S. Barison, S. Fiameni, B.E. Koel, SIMS and HR-XPS characterization of lithiated graphite from the magnetic fusion device RFX-mod, Appl. Surf. Sci. 567 (2021), 150830, https://doi.org/10.1016/j.apsusc.2021.150830.

[22] Y. Yamagishi, H. Morita, Y. Nomura, E. Igaki, Visualizing Lithium Distribution and Degradation of Composite Electrodes in Sulfide-based All-Solid-State Batteries Using Operando Time-of-Flight Secondary Ion Mass Spectrometry, ACS Appl. Mater. Interfaces 13 (2021) 580–586, https://doi.org/10.1021/acsami.0c18505.

[23] P. Hovington, V. Timoshevskii, S. Burgess, H. Demers, P. Statham, R. Gauvin, K. Zaghib, Can we detect Li K X-ray in lithium compounds using energy dispersive spectroscopy? Scanning 38 (2016) 571–578, https://doi.org/10.1002/sca.21302.

[24] J.A. Österreicher, C. Simson, A. Großalber, S. Frank, S. Gneiger, Spatial lithium quantification by backscattered electron microscopy coupled with energy-dispersive X-ray spectroscopy, Scr. Mater. 194 (2021), https://doi.org/10.1016/j.scriptamat.2020.113664.

[25] N. Ishida, H. Fukumitsu, H. Kimura, D. Fujita, Direct mapping of Li distribution in electrochemically lithiated graphite anodes using scanning Auger electron microscopy, J. Power Sources. 248 (2014) 1118–1122, https://doi.org/10.1016/j.jpowsour.2013.09.121.

[26] M. Hoffmann, M. Zier, S. Oswald, J. Eckert, Challenges for lithium species identification in complementary Auger and X-ray photoelectron spectroscopy, J. Power Sources 288 (2015) 434–440, https://doi.org/10.1016/j.jpowsour.2015.04.144.

[27] M. Hoffmann, S. Oswald, M. Zier, J. Eckert, Auger and X-ray photoelectron spectroscopy on lithiated HOPG, Surf. Interface Anal. 48 (2016) 501–504, https://doi.org/10.1002/sia.6008.

[28] S.H. Kim, S. Heo, J. Mun, G. Kim, W.J. Baek, Y.S. Kim, S. Han, H. Jung, Verification of Delayed Permanent Lithium Intercalation into Graphite Interlayers by Surface Treatment of Lithium-Ion Battery Anodes, J. Electrochem. Soc. 164 (2017) A2290–A2294, https://doi.org/10.1149/2.1411709jes.

[29] K. Kalaga, I.A. Shkrob, R.T. Haasch, C. Peebles, J. Bareño, D.P. Abraham, Auger Electrons as Probes for Composite Micro- and Nanostructured Materials: Application to Solid Electrolyte Interphases in Graphite and Silicon-Graphite Electrodes, J. Phys. Chem. C 121 (2017) 23333–23346, https://doi.org/10.1021/acs.jpcc.7b08279.

[30] E.Y. Jung, C.S. Park, J.C. Lee, E. Pazhetnov, K.J. Suh, S. Heo, T.E. Hong, D.H. Lee, S. Il Chien, H.S. Tae, Experimental study on solid electrolyte interphase of graphite electrode in Li-ion battery by surface analysis technique, Mol. Cryst. Liq. Cryst. 663 (2018) 158–167, https://doi.org/10.1080/15421406.2018.1470709.

[31] S. Hofmann, Auger- and X-Ray Photoelectron Spectroscopy in Materials Science, Springer Berlin Heidelberg, Berlin, Heidelberg, 2013. 10.1007/978-3-642-27381-0.

[32] S. Oswald, Auger-and X-ray Photoelectron Spectroscopy at Metallic Li Material: Chemical Shifts Related to Sample Preparation, Gas Atmosphere, and Ion and Electron Beam Effects, Batteries 8 (2022), https://doi.org/10.3390/batteries8030024.

[33] R.E. Clausing, D.S. Easton, G.L. Powell, Auger spectra of lithium metal and lithium oxide, Surf. Sci. 36 (1973) 377–379, https://doi.org/10.1016/0039-6028(73)90268-9.

[34] Y. Zhang, W. Zhai, X. Hu, Y. Jiang, S. Chen, Y. Zhang, W. Liu, Y. Yu, Application of Auger electron spectroscopy in lithium-ion conducting oxide solid electrolytes, Nano Res. 3 (2022) 1–10, https://doi.org/10.1007/s12274-022-4431-2.

[35] S. Craig, G.L. Harding, R. Payling, Auger lineshape analysis of carbon bonding in sputtered metal-carbon thin films, Surf. Sci. 124 (1983) 591–601.

[36] K. Ji, J. Han, A. Hirata, T. Fujita, Y. Shen, S. Ning, P. Liu, H. Kashani, Y. Tian, Y. Ito, J.I. Fujita, Y. Oyama, Lithium intercalation into bilayer graphene, Nat. Commun. 10 (2019) 1–10, https://doi.org/10.1038/s41467-018-07942-z.

[37] J.S. Murday, B.I. Dunlap, F.L. Hutson, P. Oelhafen, Carbon KVV Auger line shapes of graphite and stage-one cesium and lithium intercalated graphite, Phys. Rev. B 24 (1981).

[38] M. Endo, Y. Ahm Kim, Applications of Advanced Carbon Materials to the Lithium Ion Secondary Battery, Elsevier Ltd, 2003. 10.1016/B978-008044163-4/50025-5.

[39] B.J. Wicks, R.A. Coyle, Microstructural inhomogeneity in carbon fibres, J. Mater. Sci. 11 (1976) 376–383, https://doi.org/10.1007/BF00551449.

[40] V. Serin, R. Fourmeaux, Y. Kihn, J. Sevely, M. Guigon, Nitrogen distribution in high tensile strength carbon fibres, Carbon N. Y. 28 (1990) 573–578, https://doi.org/10.1016/0008-6223(90)90055-4.

[41] S. Nunna, C. Creighton, N. Hameed, M. Naebe, L.C. Henderson, M. Setty, B.L. Fox, Radial structure and property relationship in the thermal stabilization of PAN precursor fi bres, Polym. Test. 59 (2017) 203–211, https://doi.org/10.1016/j.polymertesting.2017.02.006.

[42] Y. Liu, Y. Zhu, Y. Cui, Challenges and opportunities towards fast-charging battery materials, Nat. Energy 4 (2019) 540–550, https://doi.org/10.1038/s41560-019-0405-3.

[43] W. Bao, J. Wan, X. Han, X. Cai, H. Zhu, D. Kim, D. Ma, Y. Xu, J.N. Munday, H. D. Drew, M.S. Fuhrer, L. Hu, Approaching the limits of transparency and conductivity in graphitic materials through lithium intercalation, Nat. Commun. 5 (2014) 1–9, https://doi.org/10.1038/ncomms5224.

[44] S.J. An, J. Li, C. Daniel, D. Mohanty, S. Nagpure, D.L. Wood, The state of understanding of the lithium-ion-battery graphite solid electrolyte interphase (SEI) and its relationship to formation cycling, Carbon N. Y. 105 (2016) 52–76, https://doi.org/10.1016/j.carbon.2016.04.008.

[45] B. Langelier, X. Wang, K. Grandfield, Atomic scale chemical tomography of human bone, Sci. Rep. 7 (2017) 1–9, https://doi.org/10.1038/srep39958.

[46] S.T. Jackson, R.G. Nuzzo, Determining hybridization differences for amorphous carbon from the XPS C 1s envelope, Appl. Surf. Sci. 90 (1995) 195–203, https://doi.org/10.1016/0169-4332(95)00079-8.

[47] I. Montero, L. Galán, A. Laurent, J. Perrière, J. Spousta, X-ray photoelectron spectroscopy and X-ray-excited Auger electron spectroscopy studies of the initial deposition of hydrogenated amorphous carbon, Thin Solid Films 228 (1993) 72–75, https://doi.org/10.1016/0040-6090(93)90567-9.

[48] J.C. Lascovich, S. Scaglione, Comparison among XAES, PELS and XPS techniques for evaluation of Sp2 percentage in a-C:H, Appl. Surf. Sci. 78 (1994) 17–23, https://doi.org/10.1016/0169-4332(94)90026-4.

[49] Y. Fang, A.J. Smith, R.W. Lindström, G. Lindbergh, I. Furó, Quantifying lithium lost to plating and formation of the solid-electrolyte interphase in graphite and commercial battery components, Appl. Mater. Today 28 (2022), https://doi.org/10.1016/j.apmt.2022.101527.